



|                                  |  |
|----------------------------------|--|
| <b>Publication Year</b>          | 2020   |
| <b>Acceptance in OA</b>          | 2022-06-17T13:35:40Z   |
| <b>Title</b>                     | Turbulence Power Spectra in Regions Surrounding Jupiter's South Polar Cyclones From Juno/JIRAM   |
| <b>Authors</b>                   | Moriconi, M. L., MIGLIORINI, Alessandra, ALTIERI, FRANCESCA, ADRIANI, Alberto, MURA, Alessandro, Orton, G., Lunine, J. I., GRASSI, Davide, Atreya, S. K., Ingersoll, A. P., Dinelli, B. M., Bolton, S. J., Levin, S., TOSI, Federico, NOSCHESE, RAFFAELLA, Plainaki, C., CICHETTI, ANDREA, Sindoni, G., Olivieri, A. |
| <b>Publisher's version (DOI)</b> | 10.1029/2019JE006096   |
| <b>Handle</b>                    | <a href="http://hdl.handle.net/20.500.12386/32394">http://hdl.handle.net/20.500.12386/32394</a>  |
| <b>Journal</b>                   | JOURNAL OF GEOPHYSICAL RESEARCH (PLANETS)  |
| <b>Volume</b>                    | 125  |

# Power spectrum analysis out of the big cyclones' circulation at Jupiter's South Pole by Juno/JIRAM data

M.L.Moriconi<sup>1</sup>, A. Migliorini<sup>2</sup>, F. Altieri<sup>2</sup>, A. Adriani<sup>2</sup>, A. Mura<sup>2</sup>, G. Orton<sup>3</sup>, J. I. Lunine<sup>4</sup>, D. Grassi<sup>2</sup>, S. K. Atreya<sup>5</sup>, A. P. Ingersoll<sup>6</sup>, B. M. Dinelli<sup>1</sup>, S. J. Bolton<sup>7</sup>, S. Levin<sup>3</sup>, F. Tosi<sup>2</sup>, R. Noschese<sup>2</sup>, C. Plainaki<sup>8</sup>, A. Cicchetti<sup>2</sup>, G. Sindoni<sup>8</sup> and A. Olivieri<sup>8</sup>.

<sup>1</sup>CNR-Istituto di Scienze dell'Atmosfera e del Clima, Bologna, Italy

<sup>2</sup>INAF-Istituto di Astrofisica e Planetologia Spaziali, Rome, Italy

<sup>3</sup>Jet Propulsion Laboratory, California Institute of Technology, 4800 Oak Grove Drive Pasadena, CA 91109 USA

<sup>4</sup>Cornell University, 410, Thurston Avenue, NY 14850-2488 USA

<sup>5</sup>University of Michigan, Climate and Space Sciences and Engineering Department, Ann Arbor, MI 48109 USA

<sup>6</sup>California Institute of Technology, 1200 E. California Blvd., Pasadena, CA 91125 USA

<sup>7</sup>Southwest Research Institute, 6220 Culebra Road, San Antonio, TX 78238 USA

<sup>8</sup>Agenzia Spaziale Italiana, Via del Politecnico snc, 00133 Roma, Italy

## Key Points:

- Dynamics consistent with quasi-geostrophic two-dimensional turbulence in the South Pole regions outside the main cyclonic circulations.
- Baroclinic instabilities can exist in these regions.
- Many waves are present in the South Pole region.

## Abstract

We present a power spectral analysis of two narrow annular regions near Jupiter's South Pole derived from data acquired by the Jovian Infrared Auroral Mapper (JIRAM) instrument onboard NASA's Juno mission. In particular, our analysis focuses on the dataset acquired by the JIRAM M-band imager (hereafter IMG-M) that probes Jupiter's thermal emission in a spectral window centered at 4.8  $\mu\text{m}$ . We analyze the power spectral densities of circular paths outside and inside of cyclones on images acquired during six Juno perijoves (PJ). The typical spatial resolution is around 55 km pixel<sup>-1</sup>. We limited our analysis to six acquisitions of the South Pole. The power spectral densities both outside and inside the circumpolar ring seem to follow two different power laws. The wavenumbers follow average power laws of  $-0.9 \pm 0.2$  (inside) and  $-1.2 \pm 0.2$  (outside), and of  $-3.2 \pm 0.3$  (inside) and  $-3.4 \pm 0.2$  (outside), respectively beneath and above the transition in slope located at  $\sim 2. \times 10^{-3}$  km<sup>-1</sup> wavenumber. This kind of spectral behavior is typical of two-dimensional turbulence. We interpret the scale corresponding to the transition in slope as the Rossby deformation radius. It is compatible with the dimensions of a subset of eddy features visible in the regions analyzed, suggesting that a baroclinic instability may exist. If so, it means that the quasi-geostrophic approximation is valid in this context.

## 37 **Plain Language Summary**

38 Juno has revealed extraordinary and unexpected dynamics in Jupiter's polar regions. The cloud  
39 patterns imaged in the infrared and visible parts of the spectrum by, respectively JIRAM and  
40 JunoCam, are organized around a central cyclone in regular patterns of eight (North Pole) and five  
41 (South Pole) cyclones. We studied the spatial and temporal variability of the regions immediately  
42 outside the cyclonic circulations at the South Pole. By analyzing multiple JIRAM images at 5  
43 microns, merged geographically and appropriately filtered and sampled, we found that the cloud  
44 patterns over Jupiter's South Pole, inside and outside the ring of cyclones, can originate in  
45 instabilities of the flow that gains their energy from motions due to horizontal pressure and  
46 temperature gradients rather than from cyclonic circulations and their interactions.

47

48 **Keywords:** Jupiter; Planetary atmospheres; Polar regions; Turbulence; Fourier analysis

49

## 50 **1. Introduction**

51 The design of Juno's orbital tour permitted the detailed observation of Jupiter's hitherto  
52 unexplored polar regions. In particular, infrared and visible observations obtained by JIRAM and  
53 JunoCam instruments, respectively (Adriani et al., 2019, 2018; Orton et al., 2017), revealed an  
54 unexpected cluster of cyclones organized in a polygonal array, time persistent during the Juno  
55 orbits. The dynamics at the root of this configuration, which is unique in the Solar System, are not  
56 yet completely understood, though certain recent studies provide some hint of the possible  
57 underlying mechanisms (Reinaud, 2019; Brueshaber et al., 2019). Power spectral analysis  
58 previously has been used to study aspects of the dynamical mechanisms operating at various  
59 scales on cloud patterns of various planetary atmospheres (Travis, 1978; Harrington et al., 1996;  
60 Peralta et al., 2007; Barrado-Izagirre et al., 2009; Choi & Showman, 2011; Cosentino et al., 2017,  
61 Young & Read, 2017, Cosentino et al., 2019). Power spectral density is a practical way to capture  
62 the statistics of cloud fields over a large scale interval and can quantify the type of turbulence  
63 acting in the atmosphere by describing the distribution of energy at various scales across the  
64 Fourier components. The study of atmospheric kinetic energy transfer, implicit in the power  
65 spectrum, generally requires the wind field measurement to have an accuracy better than 5 m/sec  
66 (Sada et al., 1996; Travis, 1978), a goal that is very difficult to achieve over large areas by the  
67 instruments onboard current space missions. However, the connection between power spectra of  
68 cloud opacities/albedo and those of atmospheric kinetic energy, empirically established by Travis  
69 (1978), has been assumed in many previous studies (Harrington et al., 1996; Peralta et al., 2007;  
70 Barrado-Izagirre et al., 2009; Choi & Showman, 2011; Cosentino et al., 2017, Young & Read,  
71 2017, Cosentino et al., 2019).

72 A puzzling question raised by the unexpected dynamical configuration of Jupiter's poles is  
73 whether the cluster of polar vortices observed by JIRAM and JunoCam is tied to a deep magneto-

74 hydrodynamic circulation, or instead is a more or less stable configuration in the weather layer  
75 supported by energy forcing from moist convection or other energy transport mechanisms  
76 (Sánchez-Lavega & Heimpel, 2018). Both the deep-convection and shallow-water models, with  
77 hybrid combinations, have been developed as general circulation hypotheses in past years  
78 (Sánchez-Lavega & Heimpel, 2018, and references therein), aiming initially to reproduce Jupiter’s  
79 banded aspect and velocities of its jets. None of these models simulated the possible dynamical  
80 structure of the polar regions. We believe that it is premature to confidently assert which of these  
81 models works better to explain the Jupiter’s poles, as observed by Juno/JIRAM. Our goal in this  
82 work is to investigate what kind of dynamics prevails in those polar regions out of the main  
83 cyclonic circulations. While one of the full polar cyclones is analyzed in the companion paper of  
84 Adriani et al. (2019) by using 2D Fourier filtering, here we use 1D Fourier spectral analysis to  
85 investigate if the dynamics in areas surrounding the main cyclones are compatible with quasi-  
86 geostrophic two-dimensional turbulence. We aim also to determine whether any changes in eddy  
87 statistics occurred between the several-month-long intervals when JIRAM observed the whole  
88 polar region. Two-dimensional turbulence is typical of large-scale motions of geophysical fluids in  
89 a shallow-water scenario (Danilov & Gurarie, 2000), and this model has been already successfully  
90 tested in the case of Jupiter’s middle and low latitudes in past years (Harrington et al., 1996;  
91 Barrado-Izagirre et al., 2009; Choi & Showman, 2011; Cosentino et al., 2017, Young & Read,  
92 2017, Cosentino et al., 2019). In our case, we have large horizontal coverage associated with a  
93 depth of sounding as yet unknown and dependent on the vertical extent and optical depth of the  
94 cloud layers that constitute the pattern imaged by JIRAM.

95 For a clear atmosphere, the whole thickness of JIRAM penetration (~150 km) related to the  
96 circumference relative to 87°S planetographic latitude (~25000 km) would give a scale  $O(10^2)$ ,  
97 thus a larger emphasis of the horizontal respect to the vertical scale. However, from a dynamical  
98 point of view, whether a phenomenon is to be considered a large-scale one depends on how much  
99 it is influenced by the planet’s rotation, as well as on its size. Therefore, the choice of the  
100 brightness scans, from which we extract signal samples to analyze, is a complicated matter. The  
101 cluster of cyclones (Adriani et al., 2018) could well have its origin deeper than the weather layer,  
102 in the light of current knowledge, while the regions outside and inside the circumpolar ring of  
103 cyclones are probably confined at some level in the weather layer. For this reason, we oriented our  
104 study to signals sampled in those regions. This has been accomplished by tracing some *ad hoc*  
105 circular paths, outside and inside the cyclonic ring (Figure 1), from which we extracted radiance  
106 signal samples. Henceforth we will refer to these two annular regions also as “equatorward” and  
107 “poleward” respectively, with respect to the ring of cyclones. Because small vortices are  
108 ubiquitous in the regions under study and they can influence the power spectral slopes (Barrado-  
109 Izagirre et al., 2009), paths have been traced in areas as uniform as possible, as explained in detail  
110 in section 2, minimizing the presence of the small vortices.

111 This work is organized into five sections. In section 2 we provide information on the instrument  
112 and describe the observations and the processing applied in order to obtain the mosaic of the entire  
113 polar region. We outline also the criteria used to select the sample data to analyze. In section 3, we

114 give details of the analysis carried out and summarize the principal results that are discussed in  
 115 section 4 in terms of models and previous turbulence results. A summary of our conclusions is  
 116 reported in section 5.

117

## 118 2. Data and methodology

119 JIRAM combines an infrared imager and a slit spectrometer, sharing the same telescope. The  
 120 imager focal plane is in turn divided into two equal areas defined by the superimposition of two  
 121 different band-pass filters: the L-filter, centered at  $3.45\ \mu\text{m}$  with a  $290\ \text{nm}$  bandwidth (IMG-L),  
 122 and the M-filter, centered at  $4.78\ \mu\text{m}$  with a  $480\ \text{nm}$  bandwidth (IMG-M). The spectrometer  
 123 covers the spectral region from  $2$  to  $5\ \mu\text{m}$  (average spectral sampling  $9\ \text{nm}/\text{band}$ ) with a  $256$  pixels  
 124 slit, co-located in the M-filter imager's Field of View (FOV) (Adriani et al., 2014).

125 Juno's highly elliptical  $\sim 53$  day polar orbit around Jupiter makes it possible to acquire very close  
 126 snapshots of the polar regions by JunoCam and JIRAM. During the spacecraft passages over

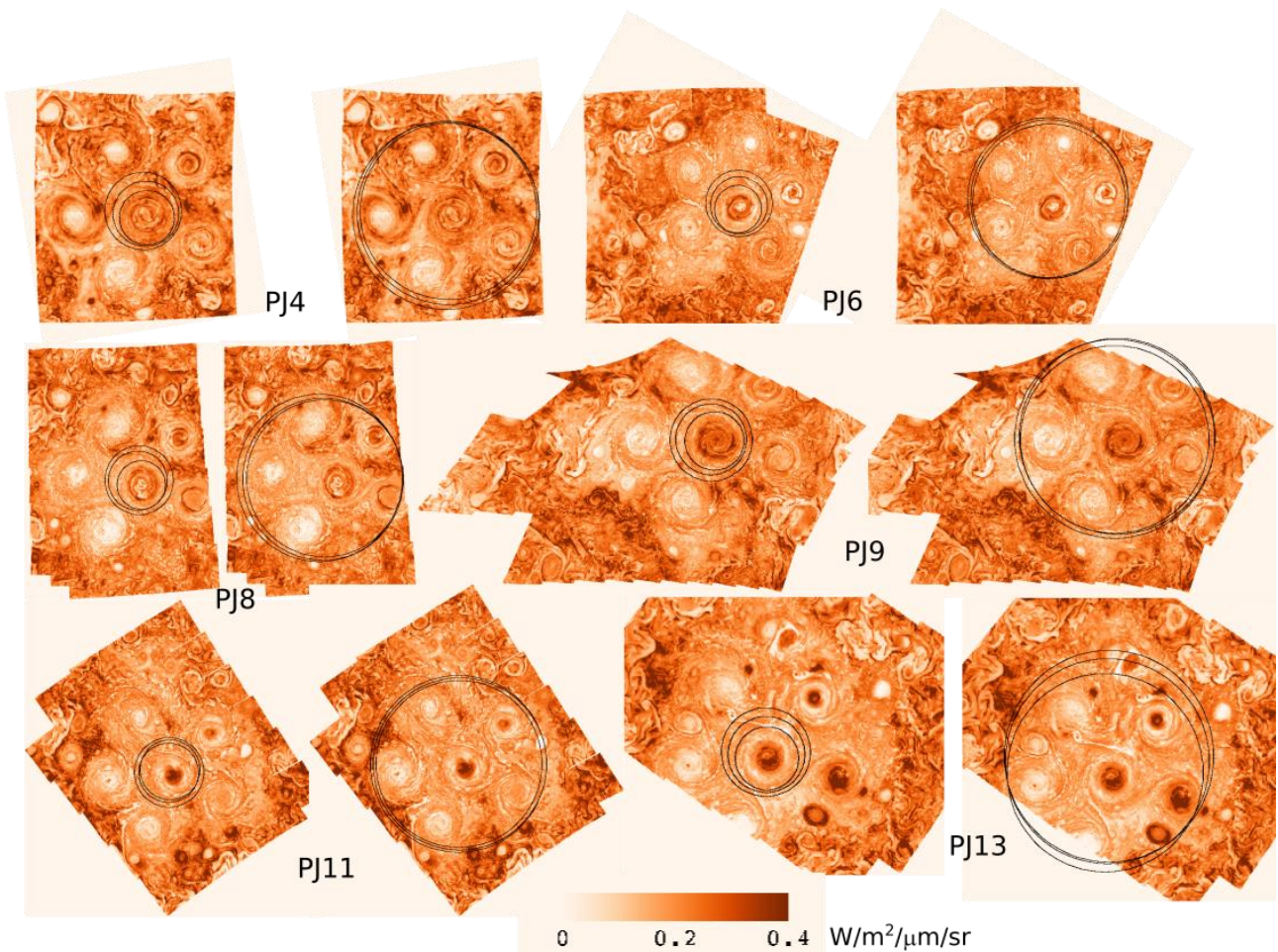


Figure 1- Stereographic projections of mosaics composed with images of Jupiter's South Pole acquired by IMG-M in six Juno perijoves. All the images have been corrected for the emission angle and re-scaled in the same range of radiance values, reported in the color bar at the bottom of the figure. Black circles indicate the trajectories along which the analyzed signals have been sampled.

127 Jupiter's poles, the instruments have the opportunity to sense adjacent regions of the underlying  
128 cloud deck. In some passages JIRAM had the opportunity to cover almost completely the polar  
129 regions. IMG-M acquired data sessions at approximately 10-minute time steps, wherein every  
130 session is a collection of observations acquired every  $\sim 30$  s. In this work, we use the images of  
131 the South Pole acquired during the fourth, sixth, eighth, ninth, eleventh and thirteenth orbits (PJ4,  
132 PJ6, PJ8, PJ9, PJ11 and PJ13 passages), spanning an overall period of roughly 1.5 years. These  
133 datasets provide full coverage from the  $82.5^\circ$  S planetographic latitude poleward, except the PJ9  
134 and PJ13 cases, where a small area is missing. Unfortunately, the spacecraft attitude did not permit  
135 the complete coverage of the northern regions during the same orbits and the North Pole had only  
136 a partial coverage, except for the PJ4 passage. Therefore, we prefer to limit our investigation to the  
137 South Pole. A list of IMG-M image sequences used in this study along with the proper pixel  
138 resolution (km) and time coverage for each sequence is reported in Supplemental Material 1.

139 In principle, JIRAM can sound atmospheric pressure levels as large as 5 bar (Kunde et al., 1982;  
140 Irwin et al., 2001, Grassi et al., 2017) in absence of thick opaque clouds, whereas in areas where  
141 thick cloud cover blocks the thermal emission from the deeper warmer interior JIRAM senses the  
142 cooler temperatures of the cloud top. All the single images by IMG-M, used to create the mosaics,  
143 have been corrected for the emission angle (that is the angle formed by the instrument line of sight  
144 and the nadir direction) and then re-projected in stereographic maps to the worst pixel resolution,  
145 that is the instantaneous FOV (IFOV) of the farthest observation of IMG-M ( $\sim 55$  km pixel<sup>-1</sup>).  
146 Projected images are shown in Figure 1. We generated six mosaics for the South Pole on  
147 geographical basis, by using geometric information derived through SPICE-based routines  
148 (<http://naif.jpl.nasa.gov>) and navigational databases (Acton, 1996), and ENVI tools  
149 (<https://www.harrisgeospatial.com/Software-Technology>) for each of the geometric calibrations  
150 and image processing applied to the JIRAM images. All the maps are based on Jupiter's  
151 planetographic latitude and System III longitudes, but with longitude increasing eastward (0-360).  
152 All the images used to create the mosaics (see Table T1 as Supporting Information) have been  
153 acquired in a time interval where, at the mean flow estimated velocity (Grassi et al., 2018), any  
154 possible cloud displacement is below the pixel resolution. The data range of the six South Pole  
155 mosaics has been adjusted to be in the same interval of radiance values and a color scale has been  
156 used to highlight the different optical depths, with the lowest radiance value in white and the  
157 highest one in orange (Figure 1). Hence, we show white cold clouds on an orange hot background.

158 We use power spectra to characterize the statistics of cloud opacities outside and inside the  
159 circumpolar ring of cyclones. These two regions have similarities from a dynamical viewpoint:  
160 both of them are marked by low wind speeds but nevertheless various morphological structures  
161 seem to suggest they are "active". The equatorward region is characterized by the interaction of  
162 the circumpolar vortices with chaotic eddy patterns outside the ring and by the mutual interplay of  
163 the vortices themselves. Similarly, the poleward region is the interaction field between the central  
164 and circumpolar cyclonic circulations. Although very low flow velocities seem to characterize  
165 these areas (at the limit of the minimum detectable wind, Grassi et al., 2018), they do not give the  
166 impression of being inactive (Figure 1): streams of thinning and thickening clouds and small

167 isolated eddies are clearly visible. Therefore, we investigated these areas using power spectral  
 168 analysis to characterize the resulting cloud statistics and to verify if the behavior is consistent with  
 169 a 2D turbulence, as reported in Harrington et al. (1996), Barrado-Izagirre et al. (2009), Choi &  
 170 Showman (2011), Cosentino et al. (2017), Young & Read (2017), Cosentino et al., (2019) for  
 171 regions at lower latitudes.

172 We extracted from each mosaic six circular samples (black circles in Figure 1), three outside and  
 173 three inside the vortex ring, which we take to be the annular region enclosing the main cyclonic  
 174 circulations. We calculated the power spectrum for every sample, then, to reduce the noise, we  
 175 produced two mean power spectra for the equatorward and for the poleward triplet by averaging  
 176 on each single triplet power spectrum. More details on the calculations are given in section 3.  
 177 Circular paths are advantageous because they combine suitable data size with the continuity of the  
 178 sample, which is periodic, assuring the stationarity of the series (Bendat & Piersol, 1986). Each  
 179 circular path has been shaped on latitude circles that vary from  $-82.5^\circ$  to  $-83.5^\circ$  for the  
 180 equatorward area, and from  $-87^\circ$  to  $-88^\circ$  for the poleward one. These paths then had to be moved  
 181 from the original latitude grid into the areas previously selected for the analysis, because of the  
 182 asymmetry of the polygon of cyclones related to the geographical pole position. Particular care has  
 183 been taken to avoid overlapping with the cyclones' edges, that we identify as those regions where  
 184 the average intensity of the azimuthal wind is larger than  $\sim 50 \text{ m sec}^{-1}$  (Grassi et al., 2018).

185 Equatorward paths from PJ9 and PJ13 enclose a small region outside the mosaic. We assume for  
 186 these cases that the series are still stationary, like those with continuous paths, basing this  
 187 assumption on similarity considerations.

188 The signals so produced are spatial series of pixel radiances as a function of the cumulative  
 189 distance from an arbitrary starting point (pixel 1) up to the last point before pixel 1 on the circular  
 190 path.

191

### 192 **3. Power Spectral Analysis**

193 We compute the power spectra of Jupiter's cloud opacities at the South Pole applying the Fast  
 194 Fourier Transform (FFT) method to the datasets sampled on each circular path shown in Figure 1.  
 195 However, because the FFT needs evenly sampled series, we resampled our datasets at even steps,  
 196 applying to every sample an algorithm performing a series of weighted-least squares fits, with  
 197 Gaussian weights, operating on a spatial grid equal to the IFOV ( $\sim 55 \text{ km pixel}^{-1}$ ) in a moving  
 198 window across the data. In Figure S2 of Supplemental Material 2 the PJ9 equatorward brightness  
 199 scan is reported, before and after the resampling operation, as an example. The residuals from the  
 200 comparison, reported as difference between the sample data value and the ones predicted from the  
 201 fit, are also shown.

202 The resulting signals have been tested for stationarity (Bendat & Piersol, 1986), searching for the  
 203 presence of a possible trend in the spatial series, although the choice of the circular path should

204 ensure no trends. This test gave negative results, confirming the correctness of our assumption of  
 205 stationarity. In view of the successive average operation to reduce spectral noise, the spatial series  
 206 have been standardized by removing the sample mean. To reduce the side-band leakage effects we  
 207 applied the Hanning tapering window (Bendat & Piersol, 1986) to every power spectrum. Then we  
 208 normalized for the variances of the signals and zero-padded all the sample data to the  $2^{11}$  constant  
 209 value, to ensure uniformity in length and bin size of the wavenumber range, thus making the  
 210 single power spectra suitable for averaging. Because all these operations do not modify the  
 211 spectral behavior, they have no impact on the principal aim of this study. The power spectra that  
 212 we obtain are functions of the wavenumber ( $\text{km}^{-1}$ ) and are plotted in logarithmic scale to highlight  
 213 the potential presence of power-law relationships in the inertial sub-range region of the spectrum.  
 214 Finally, we computed average power spectra for the regions outside and inside the circumpolar  
 215 ring. In Figure 2 we show the average power spectral density (psda hereafter) of the signals  
 216 outside the circumpolar ring, relative to the PJ4 passage. The error bars on the spectral curve are  
 217 the standard error of the mean  $\sigma_a = \sigma/\sqrt{N}$  (Bevington & Robinson, 1992). By a simple visual  
 218 inspection, the psda of Figure 2 seems to show two different slopes. To verify this hypothesis, we  
 219 wrote an algorithm for fitting two independent slopes, one at low and one at high wavenumbers,  
 220 following the approach of Choi and Showman (2011). Similar to their work, our algorithm finds  
 221 the best power-law relationships through linear least-squares fitting, constraining only the starting  
 222 and the final wavenumbers, and it determines the location of the wavenumber where the possible  
 223 transition in slope occurs by calculating the two independent best-fit slopes for each possible

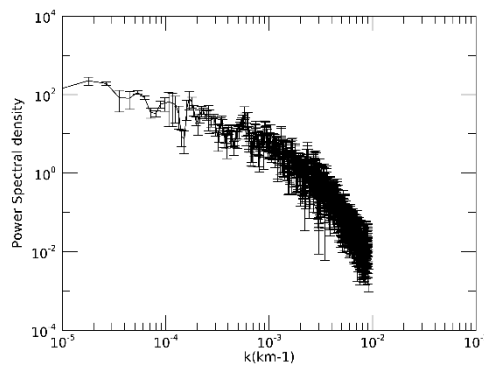
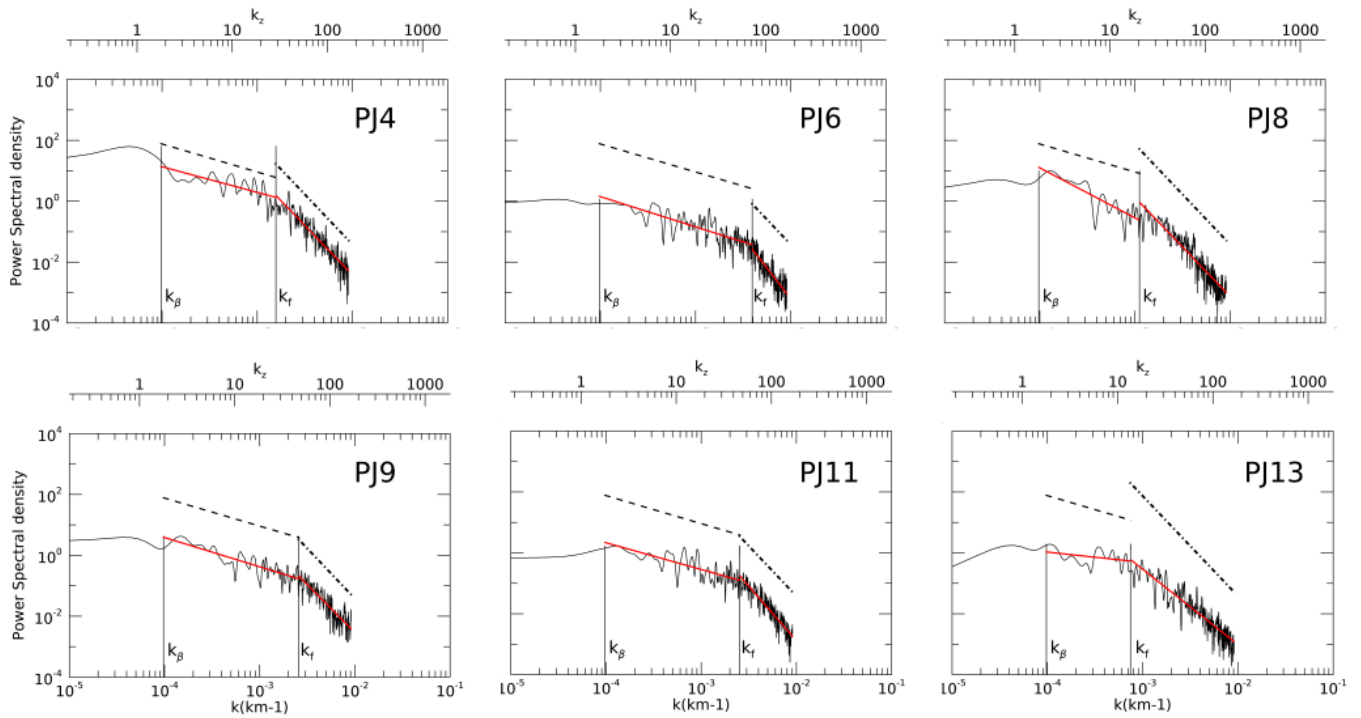


Figure 2- Average of three power spectral densities relative to the signals sampled outside the southern circumpolar ring of cyclones during PJ4. The error bars represent the standard error of the mean.

224 transition point in the wavenumber range. The overall best fit is the one with the lowest  $\chi^2 = \chi_1^2 +$   
 225  $\chi_2^2$ . In Figure S3 of Supplemental Material 2 the  $\chi^2$  relative to Figure 3 plots are shown.

## Poleward



## Equatorward

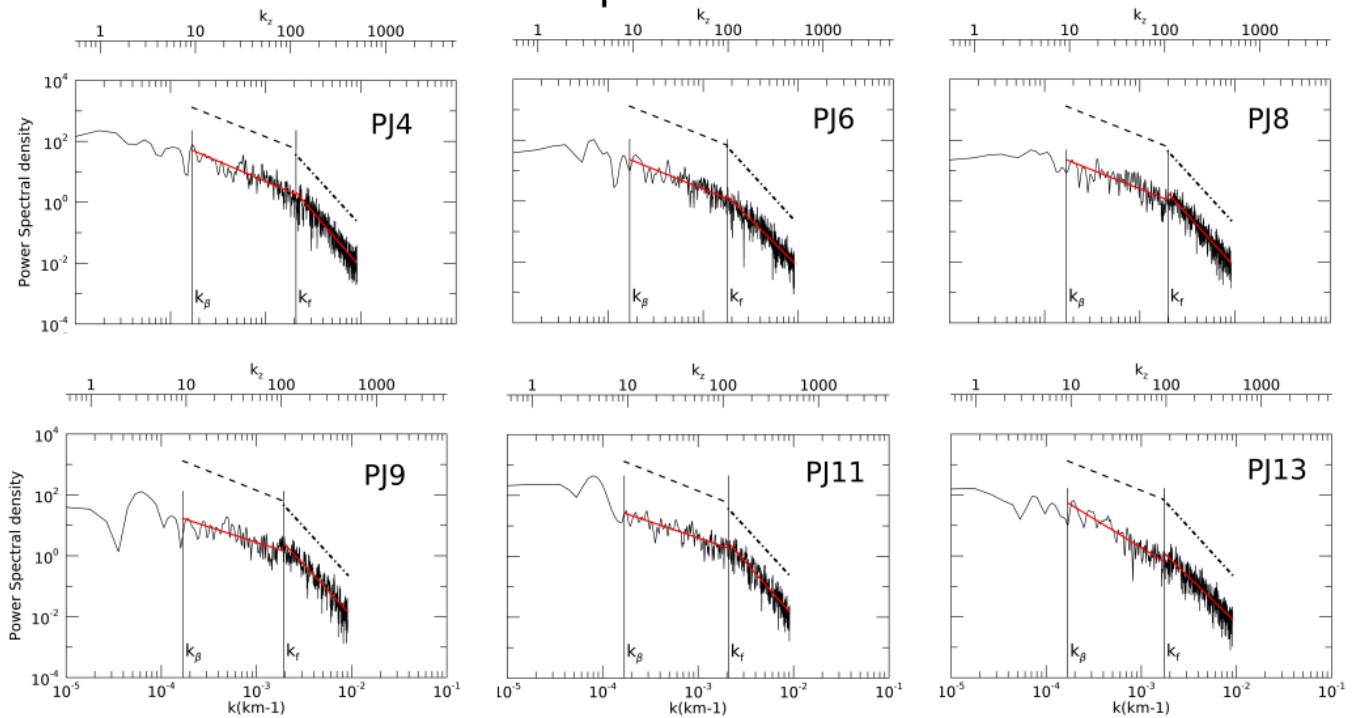


Figure 3- Averages of power spectra of the signals sampled inside (top) and outside (bottom) the southern circumpolar ring of cyclones. Power law fits overlap the spectra (red line). Median values of the overall power laws for the two cases are shown above the spectra (dashed black lines). The positions of the wavenumbers corresponding to the Rhines scale and to the transition in slope are marked by vertical lines. X axes at bottom of each plot are in wavenumbers – inverse of length – while x axes at the top are in zonal wavenumbers, as defined in the text.

227 The maximum wavenumber of the whole best-fit range is fixed by the Nyquist theorem, but the  
 228 minimum value is not so easy to constrain. In past works (Harrington et al., 1996; Barrado-  
 229 Izagirre et al., 2009; Choi and Showman, 2011), different values have been assumed on the basis  
 230 of the particular context, type of measurements and specific objectives of the research. In our  
 231 study, we test the hypothesis that the interacting regions of the polar cyclones exhibit a dynamical  
 232 state compatible with quasi-geostrophic two-dimensional turbulence, characterized by the  
 233 conservation of the potential vorticity (PV) and small Rossby number (Pedlosky, 1986). This  
 234 hypothesis makes straightforward the identification of the beginning of the power-law at low  
 235 wavenumbers with the end of the inverse cascade inertial range. Thus, we constrain the starting  
 236 value of the variation range of the overall best fit with the wavenumber value corresponding to the  
 237 Rhines scale (Rhines, 1975; Ingersoll et al., 2004)

$$k_{\beta} = \sqrt{\frac{\beta}{2U}}$$

238 where  $U$  is a typical value of the horizontal wind velocity,  $\beta = 2\Omega \cos(\varphi)/R$  is the local  
 239 derivative

| <b>Poleward</b>          |                |                |  |
|--------------------------|----------------|----------------|--|
| <b>Perijove's passes</b> | <b>Slope 1</b> | <b>Slope 2</b> | <b>Transition wavenumber (km<sup>-1</sup>)</b> |
| <b>Pj4</b>               | -0.8±0.3       | -3.2±0.3       | 1.6e-03  |
| <b>Pj6</b>               | -0.8±0.2       | -3.7±0.9       | 3.9e-03  |
| <b>Pj8</b>               | -1.6±0.5       | -3.2±0.3       | 1.1e-03  |
| <b>Pj9</b>               | -1.0±0.3       | -3.2±0.5       | 2.6e-03  |
| <b>Pj11</b>              | -0.9±0.3       | -3.6±0.5       | 2.5e-03  |
| <b>Pj13</b>              | -0.3±0.7       | -2.5±0.7       | 7.4e-04  |
| <b>median</b>            | -0.9±0.2       | -3.2±0.3       | 2.0e-03±9.3e-04                                |
| <b>Equatorward</b>       |                |                |  |
| <b>Perijove's passes</b> | <b>Slope 1</b> | <b>Slope 2</b> | <b>Transition wavenumber (km<sup>-1</sup>)</b> |
| <b>Pj4</b>               | -1.3±0.3       | -3.6±0.4       | 2.1e-03  |
| <b>Pj6</b>               | -1.3±0.4       | -3.1±0.3       | 1.8e-03  |
| <b>Pj8</b>               | -1.2±0.3       | -3.5±0.4       | 2.0e-03  |
| <b>Pj9</b>               | -1.0±0.3       | -3.4±0.3       | 1.9e-03  |
| <b>Pj11</b>              | -1.1±0.3       | -3.6±0.4       | 2.1e-03  |
| <b>Pj13</b>              | -1.9±0.3       | -3.0±0.3       | 1.7e-04  |
| <b>median</b>            | -1.2±0.2       | -3.4±0.2       | 2.0e-03±1.3e-04                                |

Table 1-Best-fit slope values for the psda of the datasets relative to different perijoves. "Poleward" and "Equatorward" table sections correspond to psda computed by signals sampled inside and outside the circumpolar ring of cyclones. We report the values of the two slopes, the 1- $\sigma$  uncertainty value for each slope fit and the wavenumber value in correspondence of the transition in slope. At the bottom of each column of the table the medians are shown.

240

241 of the Coriolis parameter with respect to the latitude  $\varphi$ , and  $\Omega$  and  $R$  are the rotation rate and the  
 242 radius of the planet. It is worthwhile mentioning that the Rhines scale may characterize many  
 243 different phenomena rather than being just the scale of the cascade arrest, as stressed in the  
 244 detailed study of Sukoriansky et al. (2007). However, in the absence of another objective criterion  
 245 that fixes the end of the linear portion of the log-log spectral curve at low wavenumbers, the  
 246 Rhines scale, intended as a sink for the energy inverse cascade (see also Cosentino et al. (2019)),  
 247 is a reasonable parameter to mark the beginning of the inertial subrange. Here, two different  $U$   
 248 values ( $20 \text{ m s}^{-1}$ ,  $15 \text{ m s}^{-1}$ ) have been assigned for equatorward and poleward regions, on the basis  
 249 of the findings of Grassi et al. (2018). The values of the Rhines scale calculated from our results  
 250 are in the range  $k \sim 1-1.5 \times 10^{-4}$ , corresponding to an interval  $\sim 2-8$  in terms of zonal  
 251 wavenumber  $k_z = \frac{2\pi R(\varphi)\cos(\varphi)}{1/k}$ . These values are very different from the ones reported in  
 252 Cosentino et al. (2019) and references therein. However, it should not be forgotten that dynamic  
 253 and thermodynamic equilibria at poles can be very different from those at mid-to-low latitudes,  
 254 where the values reported in literature have been computed. A physical interpretation of the sizes  
 255 of the structures corresponding to the limit of the inverse cascade energy is beyond the scope of  
 256 this paper.

257 Figure 3 shows the psda (black line) of the region inside (top) and outside (bottom) the  
 258 circumpolar ring of cyclones, overlain by the best-fit slopes (red line), for PJ4, PJ6, PJ8, PJ9, PJ11  
 259 and PJ13. In every plot, the positions of the Rhines parameter ( $k_\beta$ ) and of the transition in slope  
 260 ( $k_f$ ) values are also indicated on the wavenumber grid by vertical lines. In addition, we computed  
 261 the median of the best-fit slopes on all the perijove's passages in order to verify the time  
 262 variability of the single slopes, and of the  $k_f$  points. They are plotted in Figure 3 as black dashed  
 263 lines above the spectral curves.

264 As can be seen in Figure 3, the hypothesis of a double power law behavior is confirmed in most  
 265 cases, except in the PJ8 poleward region and in the PJ13 equatorward region. However, it should  
 266 be noted that both the slopes, and consequently the position of  $k_f$ , depend on the value of the best-  
 267 fit starting point. This dependence has been noted also by Cosentino et al. (2019) who investigate  
 268 it by carrying out a sensitivity study on the dependence of the position of the transition in slopes  
 269 on the  $k$  initial value. Future analyses will benefit from their detailed study.

270 We assigned to all the Rhines parameters the PJ4 value of horizontal velocity, the only one  
 271 computed so far (Grassi et al., 2018), but this choice is not obvious. Small variations of  $U$  have a  
 272 significant impact on the slope values and on the  $k_f$  position. On the other hand, the PJ4 value of  
 273 horizontal velocity seems adequate in most cases, as confirmed in Table 1, where the best-fit  
 274 values of the two slopes and the relative medians are reported for all perijoves, together with their  
 275  $1-\sigma$  uncertainty.

276 Slope values for larger scales, as can be seen in Table 1, are slightly different inside and outside  
 277 the circumpolar ring, in line with the results obtained in previous works (Harrington et al., 1996;  
 278 Barrado-Izagirre et al., 2009; Choi & Showman, 2011). Results for smaller scales are more  
 279 uniform relative to those of slope 1. However, slope 2 values appear somewhat larger than those  
 280 reported in the literature cited above. Hypotheses to explain these findings are described in section  
 281 4.

282 As shown in Table 1, the break in slope  $k_f$  exhibits more variability inside than outside the ring.  
 283 However, the median values are equal in the two cases, with uncertainties that reflect the differing  
 284 extent of variability. On the other hand, if we refer to the zonal wavenumber  $k_z$ , we obtain median  
 285 values rather different for the poleward ( $36.6 \pm 17.0$ ) and equatorward region ( $109.7 \pm 7.1$ ). These  
 286 results differ in detail from those reported in Harrington et al. (1996), Barrado-Izagirre et al.  
 287 (2009) and Choi & Showman (2011), even though they see a large variability in the  $k_f$  values.

288 Figure 3 shows also variability of the integrated power under the curves with time. Although a  
 289 detailed analysis is beyond the principal aims of our investigation, a simple visual inspection of  
 290 the plots in Figure 3 shows that contributions from the integrated radiance inside the circumpolar  
 291 ring varies with time, with the largest integrated power registered during PJ4, while this behavior  
 292 is not so evident for the integrated psda outside the ring.

293

#### 294 4. Discussion

295 The results described in the previous section come from the application of well-established  
 296 methods of data analysis, which were successfully used in the past to describe the spatial structure  
 297 of Jupiter's cloud patterns at various depths, and their relationship to turbulence (Harrington et al.,  
 298 1996; Barrado-Izagirre et al., 2009; Choi & Showman, 2011; Cosentino et al., 2017). Because  
 299 previous studies refer to mid-latitude and the equator, a comparison between those findings and  
 300 ours has little significance, considering the very different dynamical contexts. However, in both  
 301 cases the power spectra are best fitted by two slopes with similar power laws. All these slopes,  
 302 including our own values, show some deviations from the values predicted from pure 2D  
 303 turbulence theory (Kraichnan, 1967; 1971).

304 The classical 2D and 3D (Kolmogorov, 1941) turbulence equations predict different values for the  
 305 slopes of the power laws, depending on the turbulent regime. In the 3D turbulent regime there is  
 306 only one slope, the energy cascade is downscale and the energy is transferred from large to smaller  
 307 scales, with a  $k^{-5/3}$  law. The rigorous 2D theory, governed by the 2D Navier-Stokes equation,  
 308 introduces the notion of an inverse cascade of energy, or a transfer of energy from small to larger  
 309 scales beginning at the forcing wavenumber. It is applied to incompressible fluids and predicts  
 310 two inertial intervals, above and below the forcing scale, namely an inverse energy and a direct  
 311 enstrophy cascade, where the enstrophy (the integral of the square of the vorticity) accounts for  
 312 the dissipative effects arising from rotation, vortex formation and generally any swirling activity  
 313 in the flow. The upscale energy flux should give, according to the theory, a  $k^{-5/3}$  power law, while

314 the downscale enstrophy flux should give a power law with slope -3. However, large-scale  
315 geophysical flows, although nearly two-dimensional, show deviations from the predictions of  
316 strictly 2D fluid dynamics.

317 A dimensionless parameter relevant to the atmospheric dynamics and turbulence is the Rossby  
318 number  $Ro=U/fL$ , where  $U$  is the background wind speed,  $L$  is the horizontal scale of the  
319 disturbance associated with the phenomenon under study and  $f$  is the Coriolis parameter.  $Ro$  gives  
320 a measure of the significance of rotation apparent forces on the phenomenon under study.

321 In quasi-geostrophic approximation, the flow is nearly in geostrophic balance but with an inertial  
322 contribution significantly smaller than the Coriolis one ( $Ro \ll 1$ ). Indeed, the quasi-geostrophic  
323 equations, in their stream function formulation, differ from the Navier-Stokes ones for the terms  
324 depending on  $Ro^{-1}$  (Foster et al., 2103). As in the classical 2D turbulence, energy and enstrophy  
325 are conserved, but the Coriolis predominance on the inertial term makes vortex stretching  
326 possible.

327 With reference to the transition wavenumbers reported in Table 1, the horizontal length scale  
328  $L=1/k_f$ , implies for  $Ro$ , with  $f \cong 3.5 \times 10^{-4} \text{ s}^{-1}$  at polar latitudes, values in the range  $\cong 0.08 -$   
329  $0.1$ . These are compatible with the hypothesis of quasi-geostrophic 2D turbulence used in this  
330 analysis.

331 Various dissipation mechanisms can disrupt the steady-state characteristics of the turbulent  
 332 regime. Friction and wave-wave interaction, can determine transfer of energy and enstrophy in the  
 333 enstrophy and energy inertial ranges (Maltrud & Vallis, 1993; Young & Read, 2017), modifying  
 334 the expected slopes. In particular, the physical meaning of nonlinear wave-wave interactions is  
 335 that resonant sets of wave components exchange energy, redistributing it over the spectrum  
 336 (Phillips, 1960). In shallow-water models three-wave interactions (so-called triad interactions)  
 337 become important. Evidence of the influence of nonlinear triad interactions on the transfer of  
 338 kinetic energy through the whole range of length scale has been reported by Young & Read  
 339 (2017). They used datasets, acquired in the visible and near-infrared bands in December 2000  
 340 during the NASA Cassini mission, to determine the direction of Jupiter's kinetic energy cascade  
 341 throughout the range of length scales of their specific observations. They found that a transfer of  
 342 energy occurs not only upscale of the spectral “kink”, as expected in quasi-geostrophic two-  
 343 dimensional turbulence, but also downscale in a non-negligible component. Computing the  
 344 spectral fluxes of kinetic energy both directly, from two of their datasets, and by calculating  
 345 nonlinear triad interactions, from the third one, they found that eddy-eddy interactions contribute  
 346 significantly. Although this computation refers to middle-to-low latitudes, it may be considered  
 347 valid in whatever region of Jupiter presents similar conditions.

348 Figure 4 shows that many wave-like features are present on Jupiter’s South Pole, concealed by the  
 349 large-scale cloud patterns, and that some of which can interact (panel e). We intend for wave-like  
 350 feature a regular pattern of three or more alternated crests (low radiance values) and trough (high  
 351 radiance values). The hidden wavy pattern has been revealed by means of high-pass FFT filtering  
 352 (Pratt, 2001) of the image (panels c, d and e). Few notes on the working principles of the FFT  
 353 filtering (Text S1) are reported in Supplemental Material 3 and the kernel high-pass shape (Figure

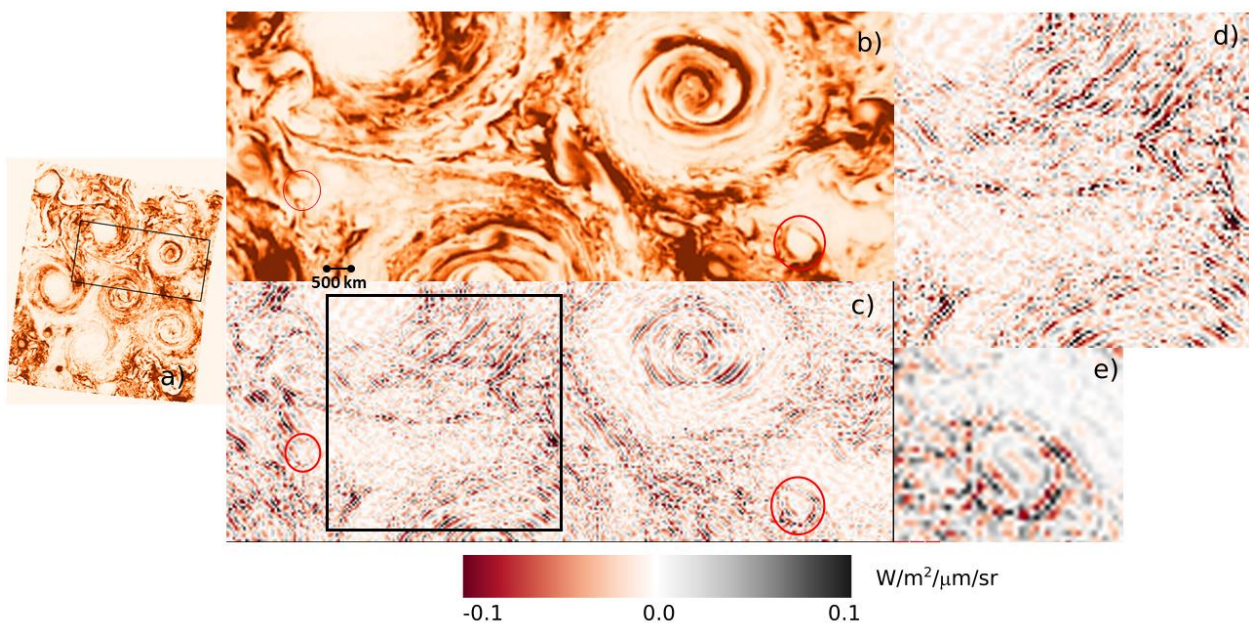


Figure 4- Visualization of Jupiter’s South Pole dynamics, from PJ4 perijove. a) Map of the whole cluster of cyclones; the panel b) position is highlighted (black rectangle); b) detail of the intermediate region, straddling the central cyclone (bottom of the panel) and two vortices of the circumpolar ring; two minor vortices are marked with red circles; c) the same of panel b), but after high-pass Fourier filtering. Many wave-like features result once the frequencies of the most evident patterns have been removed. The panel d) position is highlighted (black square) and the 500 km horizontal scale is reported above. d) and e) are details of the intermediate region and of the minor vortex at the right bottom corner of panel c). Wavy patterns of different amplitude and direction are clearly visible, some of them converging. The d) and e) panels are the enhanced contents of the areas inside the black square and the red circle in the right bottom of panel c), respectively. The colorbar applies to the c), d) and e) panels.

354 S4) in Supplemental Material 2.

355 A complete study of the origins of the wavy pattern in Jupiter's polar regions is the subject of  
 356 another paper in preparation. A different sampling strategy must be applied to the IMG-M data, to  
 357 optimize the wave analysis, and a complete overview of the various wave typologies and of the  
 358 possible implied dynamic scenarios must be done. Here we note only that the conditions for triad  
 359 interactions are present in the region studied and that this circumstance could explain the deviation  
 360 of the slopes derived in this study from the theoretical 2D power laws.

361 The  $k_f$  transition in slope, obtained in this work, indicates that a forcing scale can exist around 500  
 362 km. If we hypothesize that baroclinic instabilities play a non-negligible role in the region under  
 363 investigation, then we can assign to  $L$  the  $L_d$  Rossby deformation radius meaning (Pedlosky,  
 364 1986). It must be noted that the  $L_d$  values, reported in the Jovian literature, have been quite  
 365 different so far, with values  $O(10^3 \text{ km})$  (Harrington et al., 1996; Young & Read, 2017). However,  
 366 those values have been estimated for different pressure levels and at different latitudes. We use the  
 367 same approach as Conrath et al. (1981), that refers to data acquired during Voyagers missions of  
 368 the Jovian stratosphere, but using values of the various parameters derived from the Galileo  
 369 mission, adjusted to a tropospheric depth down to  $p_0 \cong 5 \text{ bar}$ .

370 Specifically, the deformation radius is

$$L_d = \frac{H}{f} \times N$$

371 where  $H$  is the vertical scale height,  $f$  the Coriolis parameter and  $N$  the Brunt–Väisälä (buoyancy  
 372 term) frequency.  $H$  is computed from  $H=RT/g \cong 23 \text{ km}$ , with  $T \cong 180 \text{ K}$ , calculated as the mean  
 373 between  $p_2=0.03 \text{ bar}$  (low stratosphere) and  $p_1=5 \text{ bar}$  (deepest sounding level of JIRAM)  
 374 pressure levels, the gas constant  $R=3600 \text{ J kg}^{-1} \text{ K}^{-1}$ ) and the gravity acceleration  $g=28.3 \text{ m s}^{-2}$ , at  
 375 polar latitudes.

376 The Brunt–Väisälä frequency for the troposphere assumes values ranging in the interval 0.01-  
 377  $0.006 \text{ s}^{-1}$  (Watkins & Cho, 2013; Magalhães et al., 2002). Accordingly, the Rossby deformation  
 378 radius values vary from  $L_d \sim 650 \text{ km}$  to  $L_d \sim 395 \text{ km}$ , in agreement with the median value of  $1/k_f$   
 379 (Table 1).

380 These values of  $L_d$  at Jupiter's South Pole, converted into the planetary Burger number  $Bu = \left(\frac{L_d}{R_c}\right)^2$ ,  
 381 with  $R_c$  being the polar radius of curvature, yield  $Bu \sim 0.3-0.7 \times 10^{-4}$ . The planetary Burger number  
 382 is a dimensionless parameter indicating the importance of the fluid stratification on the dynamics.  
 383 Our findings agree with the polar dynamical regime which Brushaber et al. (2019) define as  
 384 “Jupiter-like”. In this regime  $Bu \sim 10^{-4}$ , while values typical for Saturn and ice giant polar  
 385 dynamics are  $Bu \sim 10^{-3}$  and  $Bu \sim 10^{-2}$ , respectively.

386 On the other hand,  $L_d$  can be thought of as the horizontal scale at which rotation effects become as  
 387 important as buoyancy effects. Thus, if we interpret  $1/k_f$  as the Rossby deformation radius, we  
 388 expect there should be some eddies and/or meanders in the flow with the same horizontal scale of  
 389  $L_d$  in the regions under study. In Figure 4b the 500 km horizontal scale is compared with a couple  
 390 of small eddies (red circle) at the limit of the poleward region. Both of them show circular  
 391 streamlines, encircling a uniform core, and are overlaid by waves transversally oriented (Figure  
 392 4e).

393 Consequently, the comparison between the power spectrum analysis and FFT filtering of the  
 394 images suggests the presence of some baroclinic instabilities in the region sampled in this study.  
 395 We observe that this finding is compatible with a two-layer model, with horizontal gradients of  
 396 temperature parallel to isobaric contours deep in the atmosphere (equivalent barotropic  
 397 atmosphere) and a thin upper layer where temperature gradients cross the isobars and baroclinic  
 398 instabilities transfer energies from  $\sim 500$  km toward larger scales. This can be a possible scenario  
 399 if the deep atmosphere, embedded between the central cyclone and the circumpolar ring, does not  
 400 experience any mixing with warm air masses associated with the cyclonic circulations. Recently,  
 401 Aurnou et al. (2018) suggested in their gas giant convection model a similar scenario,  
 402 characterized by a thick stable layer with strong stability, and deep polar cyclones, perhaps  
 403 penetrating to the depth of the zonal jets. The low variability of the slopes in Table 1 throughout  
 404 the various perijoves suggests that this scenario persists for at least months or years.

405

## 406 5. Conclusions

407 We used a power spectrum analysis on Jupiter's polar cloud opacities to infer what type of  
 408 turbulent regime is acting on the regions just outside and inside the cluster of cyclones encircling  
 409 the South Pole. We found that the shape of the power spectra is compatible with a quasi-  
 410 geostrophic two-dimensional turbulent regime, both for the equatorward and poleward annular  
 411 regions considered here, with forcing scale around 500 km. We also found that this regime is  
 412 preserved, with few variations, in six out of ten Juno orbits around Jupiter, spanning an overall  
 413 period of roughly 1.5 years. The slight difference between the slopes in this work and the  
 414 theoretical  $k^{-5/3}$  and  $k^{-3}$  power laws can have more than one reason. The presence of minor vortices  
 415 along some brightness circular paths or dissipation mechanisms, like the triad interaction, that  
 416 redistribute energy and enstrophy on different scale ranges are two possible explanations of the  
 417 deviation from theoretical slopes. A possible hint of the triad interaction is the complex pattern of  
 418 waves revealed by processing the images with high-pass FFT filtering. In this work we assumed  
 419 that the forcing scale can be interpreted as the Rossby deformation radius, a hypothesis that would  
 420 seem to be confirmed by the presence of eddies and meanders of similar size inside the flow.  
 421 Finally, we deduce that baroclinic instabilities perturb the region under analysis. This conclusion  
 422 prompts us to speculate on a possible scenario of deep equivalent-barotropic atmosphere.  
 423 Additional insights into the puzzling deep dynamics of the Jupiter's polar atmosphere will come

424 from the findings of Juno/MWR (MicroWave Radiometer), which senses deeper levels of  
 425 Jupiter's atmosphere than does JIRAM.

426

427

## 428 **Acknowledgments and Data Statement**

429 We thank F. Bignami from Institute of Marine Sciences (CNR-Italy), A. Provenzale from Institute  
 430 of Geosciences and Earth Resources (CNR-Italy), J. von Hardenberg from Institute of  
 431 Atmospheric Sciences and Climate (CNR-Italy) and A. Bracco from the Georgia Institute of  
 432 Technology (USA) for their comments and helpful discussions. The JIRAM project is funded by  
 433 the Italian Space Agency (ASI). In particular, this work has been developed under the agreement  
 434 2016-23-H.0. Part of this research was also supported by the National Aeronautics and Space  
 435 Administration, a portion of which funding was provided to the Jet Propulsion Laboratory,  
 436 California Institute of Technology.

437 Original JIRAM data used for this work are available at the NASA Planetary Data System website

438 [https://pds-atmospheres.nmsu.edu/data\\_and\\_services/atmospheres\\_data/JUNO/jiram.html](https://pds-atmospheres.nmsu.edu/data_and_services/atmospheres_data/JUNO/jiram.html).

439 The datasets generated during the current study are available at  
 440 <http://dx.doi.org/10.17632/4f3mrkcxvb.2>.

441

## 442 **Captions**

443 Figure 1 - Stereographic projections of mosaics composed with images of Jupiter's South Pole  
 444 acquired by IMG-M in six Juno perijoves. All the images have been corrected for the emission  
 445 angle and re-scaled in the same range of radiance values, reported in the color bar at the bottom of  
 446 the figure. Black circles indicate the trajectories along which the analyzed signals have been  
 447 sampled.

448 Figure 2 - Average of three power spectral densities relative to the signals sampled outside the  
 449 southern circumpolar ring of cyclones during PJ4. The error bars represent the standard error of  
 450 the mean.

451 Figure 3 - Averages of power spectra of the signals sampled inside (top) and outside (bottom) the  
 452 southern circumpolar ring of cyclones. Power law fits overlap the spectra (red line). Median  
 453 values of the overall power laws for the two cases are shown above the spectra (dashed black  
 454 lines). The positions of the wavenumbers corresponding to the Rhines scale and to the transition in  
 455 slope are marked by vertical lines. X axes at bottom of each plot are in wavenumbers – inverse of  
 456 length – while x axes at the top are in zonal wavenumbers, as defined in the text.

457 Figure 4 - Visualization of Jupiter's South Pole dynamics, from PJ4 perijove. a) Map of the whole  
 458 cluster of cyclones; the panel b) position is highlighted (black rectangle); b) detail of the  
 459 intermediate region, straddling the central cyclone (bottom of the panel) and two vortices of the  
 460 circumpolar ring; two minor vortices are marked with red circles; c) the same of panel b), but after  
 461 high-pass Fourier filtering. Many wave-like features result once the frequencies of the most  
 462 evident patterns have been removed. The panel d) position is highlighted (black square) and the  
 463 500 km horizontal scale is reported above. d) and e) are details of the intermediate region and of  
 464 the minor vortex at the right bottom corner of panel c). Wavy patterns of different amplitude and  
 465 direction are clearly visible, some of them converging. The d) and e) panels are the enhanced  
 466 contents of the areas inside the black square and the red circle in the right bottom of panel c),  
 467 respectively. The colorbar applies to the c), d) and e) panels.

468 Table 1 – Best-fit slope values for the psda of the datasets relative to different perijoves.  
 469 “Poleward” and “Equatorward” table sections correspond to psda computed by signals sampled  
 470 inside and outside the circumpolar ring of cyclones. We report the values of the two slopes, the 1-  
 471  $\sigma$  uncertainty value for each slope fit and the wavenumber value in correspondence of the  
 472 transition in slope. At the bottom of each column of the table the medians are shown.

473

#### 474 **References**

- 475 Acton, C. H. (1996). *Ancillary data services of NASA's Navigation and Ancillary Information*  
 476 *Facility*. Planetary and Space Science, 44(1), 65–70. [https://doi.org/10.1016/0032-0633\(95\)00107-](https://doi.org/10.1016/0032-0633(95)00107-7)  
 477 [7](https://doi.org/10.1016/0032-0633(95)00107-7)
- 478 Adriani, A. et al. (2019). *Two-Years Observations of the Jupiter Polar Regions by JIRAM on*  
 479 *board Juno*". Submitted to Journal of Geophysical Research: Planets.
- 480 Adriani, A., Filacchione, G., di Iorio, T., Turrini, D., Noschese, R., Cicchetti, A., et al. (2014).  
 481 *JIRAM, the Jovian infrared auroral mapper*. Space Science Reviews, 213(1-4), 393–446.  
 482 <https://doi.org/10.1007/s11214-014-0094-y>.
- 483 Adriani, A., Mura, A., Orton, G. S., Hansen, C., Altieri, F., Moriconi, M. L., et al. (2018). *Clusters*  
 484 *of cyclones encircling Jupiter's poles*. Nature, 555(7695), 216–219.  
 485 <https://doi.org/10.1038/nature25491>.
- 486 Aurnou, J. M., Heimpel, M. H., & Featherstone, N. A. (2018). *Simulating Atmospheric Features*  
 487 *of Jupiter and Saturn With Deep Convection Models*. Paper presented at Fall Meeting 2018,  
 488 American Geophysical Union, New Orleans, Louisiana.
- 489 Barrado-Izagirre, N., Pérez-Hoyos, S., & Sánchez-Lavega, A. (2009). *Brightness power spectral*  
 490 *distribution and waves in Jupiter's upper cloud and hazes*. Icarus, 202(1), 181-196.  
 491 doi:10.1016/j.icarus.2009.02.015.

- 492 Bendat, J. S., & Piersol, A. G. (1986). *Random Data: Analysis and Measurement Procedures*.  
493 New York: Wiley, 566 pp.
- 494 Bevington, P. H., & Robinson, D. K. (1992). *Data Reduction and Error Analysis for the Physical*  
495 *Sciences*. McGraw.Hill (2<sup>nd</sup> ed.), 328 pp.
- 496 Brueshaber, S. R., Sayanagi, K. M., & Dowling, T. E. (2019). *Dynamical regimes of giant planet*  
497 *polar vortices*. *Icarus*, 323, 46-61. doi: 10.1016/j.icarus.2019.02.001.
- 498 Choi, D. S., & Showman, A. P. (2011). *Power spectral analysis of Jupiter's clouds and kinetic*  
499 *energy from Cassini*. *Icarus*, 216(2), 597-609. doi:10.1016/j.icarus.2011.10.001.
- 500 Conrath, B. J., Gierasch, P. J., & Nath, N. (1981). *Stability of Zonal Flows on Jupiter*. *Icarus*, 48,  
501 256-282.
- 502 Cosentino, R. G., Butler, B., Sault, B., Morales-Juberías, R., Simon, A., de Pater, I. (2017).  
503 *Atmospheric waves and dynamics beneath Jupiter's clouds from radio wavelength observations*.  
504 *Icarus*, 292, 168-181. doi: 0.1016/j.icarus.2017.01.006.
- 505 Cosentino, R. G., Simon, A., & Morales-Juberías (2019). *Jupiter's Turbulent Power Spectra From*  
506 *Hubble Space Telescope*. *Journal of Geophysical Research: Planets*, 124, 1204–1225.  
507 <https://doi.org/10.1029/2018JE005762>
- 508 Danilov, S. D., & Gurarie D. (2000). *Quasi-two-dimensional turbulence*. *Uspekhi Fizicheskikh*  
509 *Nauk*, 170 (9), 921 – 968. doi: 10.1070/PU2000v043n09ABEH000782.
- 510 Foster, E. L., Iliescu, T., & Wang, Z. (2013). *A Finite element discretization of the streamfunction*  
511 *formulation of the stationary quasi-geostrophic equations of the ocean*. *Comput. Methods Appl.*  
512 *Mech. Engrg.* 261–262, 105-117, <https://doi.org/10.1016/j.cma.2013.04.008>.
- 513 Grassi, D., Adriani, A., Mura, A., Dinelli, B. M., Sindoni, G., Turrini, D., et al. (2017).  
514 *Preliminary results on the composition of Jupiter's troposphere in hot spot regions from the*  
515 *JIRAM/Juno instrument*. *Geophysical Research Letters*, 44, 4615–4624. doi:  
516 10.1002/2017GL072841.
- 517 Grassi, D., Adriani, A., Moriconi, M. L., Mura, A., Tabataba-Vakili, F., Ingersoll A. P., et al.  
518 (2018). *First Estimate of Wind Fields in the Jupiter Polar Regions From JIRAM-Juno Images*.  
519 *Journal of Geophysical Research: Planets*, 123(6), 1511-1524. doi:10.1029/2018JE005555.
- 520 Harrington, J., Dowling, T.E., & Baron, R. L. (1996). *Jupiter's Tropospheric Thermal Emission*  
521 *II: Power Spectrum Analysis and Wave Search*. *Icarus*, 124, 32–44.  
522 <https://doi.org/10.1006/icar.1996.0188>.
- 523 Ingersoll, A. P., Dowling, T. E., Gierasch, P. J., Orton, G. S., Read, P. L., Sánchez-Lavega, A., et  
524 al. (2004). *Dynamics of Jupiter's Atmosphere*. in *Jupiter: The planet, satellites and magnetosphere*,  
525 Cambridge University Press, 719 pp.

- 526 Irwin, P. G. J., Weir, A. L., Taylor, F. W., Calcutt, S. B., Carlson, R. W. (2001). *The Origin of*  
 527 *Belt/Zone Contrasts in the Atmosphere of Jupiter and Their Correlation with 5  $\mu\text{m}$  Opacity.*  
 528 *Icarus*, 149(2), 397-415. doi:10.1006/icar.2000.6542.
- 529 Kolmogorov, A. N. (1941). *The local structure of turbulence in incompressible viscous fluid for*  
 530 *very large Reynolds numbers.* Doklady Akademiia Nauk SSSR, 30, 301-305.  
 531 <https://www.jstor.org/stable/51980>.
- 532 Kraichnan, R. H. (1967). *Inertial Ranges in Two-Dimensional Turbulence.* *Physics of Fluids*, 10,  
 533 1417-1422. <https://doi.org/10.1063/1.1762301>.
- 534 Kraichnan, R. H. (1971). *Inertial-range transfer in two- and three-dimensional turbulence.*  
 535 *Journal of Fluid Mechanics*, 47, 525-535. <https://doi.org/10.1017/S0022112071001216>.
- 536 Kunde, V., Hanel, R., Maguire, W., Gautier, D., Baluteau, J. P., Marten, A., et al. (1982). *The*  
 537 *tropospheric gas composition of Jupiter's north equatorial belt ( $\text{NH}_3$ ,  $\text{PH}_3$ ,  $\text{CH}_3\text{D}$ ,  $\text{GeH}_4$ ,  $\text{H}_2\text{O}$ ) and*  
 538 *the jovian D/H isotopic ratio.* *Astrophysical Journal*, 263, 443-467. doi:10.1086/160516.
- 539 Magalhães, J. A., Seiff, A., & Young, R. E. (2002). *The Stratification of Jupiter's Troposphere at*  
 540 *the Galileo Probe Entry Site.* *Icarus*, 158(2), 410-433. doi:10.1006/icar.2002.6891.
- 541 Maltrud, M. E., & Vallis, G. K. (1993). *Energy and enstrophy transfer in numerical simulations of*  
 542 *two-dimensional turbulence.* *Physics of Fluids A: Fluid Dynamics*, 5(7), 1760-1775. doi:  
 543 10.1063/1.858851.
- 544 Orton, G. S., Hansen, C., Caplinger, M., Ravine, M., Atreya, S., Ingersoll, A. P., et al. (2017). *The*  
 545 *first close-up images of Jupiter's polar regions: Results from the Juno mission JunoCam*  
 546 *instrument.* *Geophysical Research Letters*, 44, 4599-4606.  
 547 <https://doi.org/10.1002/2016GL072443>.
- 548 Pedlosky, J. (1986). *Geophysical Fluid Dynamics*, Springer (2<sup>nd</sup> ed.), 710 pp.
- 549 Peralta, J., Hueso, R., & Sánchez-Lavega, A. (2007). *Cloud brightness distribution and turbulence*  
 550 *in Venus using Galileo violet images.* *Icarus*, 188(2), 305-314. doi:10.1016/j.icarus.2006.12.005.
- 551 Phillips, O. M. (1960). *On the dynamics of unsteady gravity waves of finite amplitude.* *Journal of*  
 552 *Fluid Mechanics*, 9(2), 193-217. doi:10.1017/S0022112060001043.
- 553 Pratt, W. K. (2001). *Digital Image Processing*, John Wiley & Sons, Inc., 738 pp.
- 554 Reinaud, J. N. (2019). *Three-dimensional quasi-geostrophic vortex equilibria with m-fold*  
 555 *symmetry.* *Journal of Fluid Mechanics*, 863, 32-59. doi:10.1017/jfm.2018.989.
- 556 Rhines, P. B. (1975). *Waves and turbulence on a beta-plane.* *Journal of Fluid Mechanics*, 69(3),  
 557 417-443. <https://doi.org/10.1017/S0022112075001504>.

- 558 Sada, P. V., Beebe, R. F., & Conrath, B. J. (1996). *Comparison of the Structure and Dynamics of*  
559 *Jupiter's Great Red Spot between the Voyager 1 and 2 Encounters*. *Icarus*, 119(2), 311-335. doi:  
560 10.1006/icar.1996.0022.
- 561 Sánchez-Lavega, A., & Heimpel, M. (2018). *Atmospheric Dynamics of Giants and Icy Planets*. in  
562 *Handbook of Exoplanets*, H.J. Deeg, J.A. Belmonte (eds.), 3490 pp. doi: 10.1007/978-3-319-  
563 30648-3\_51-1.
- 564 Travis, L. D. (1978). *Nature of the Atmospheric Dynamics on Venus from Power Spectrum*  
565 *Analysis of Mariner 10 Images*. *Journal of the Atmospheric Sciences*, 35, 1584-1595.  
566 [https://doi.org/10.1175/1520-0469\(1978\)035<1584:NOTADO>2.0.CO;2](https://doi.org/10.1175/1520-0469(1978)035<1584:NOTADO>2.0.CO;2)
- 567 Watkins, C., & Cho, J. Y-K. (2013). *The vertical structure of Jupiter's equatorial zonal wind*  
568 *above the cloud deck, derived using mesoscale gravity waves*. *Geophysical Research Letters*,  
569 40(3), 472-476, doi:10.1029/2012GL054368.
- 570 Young, R. M. B., & Read, P. L. (2017). *Forward and inverse kinetic energy cascades in Jupiter's*  
571 *turbulent weather layer*. *Nature Physics*,13, 1135-1142. doi: 10.1038/NPHYS4227.

## Poleward

| Perijove's passes | Slope 1  | Slope 2  | Transition wavenumber (km <sup>-1</sup> ) |
|-------------------|----------|----------|---|
| Pj4               | -0.8±0.3 | -3.2±0.3 | 1.6e-03                                   |
| Pj6               | -0.8±0.2 | -3.7±0.9 | 3.9e-03                                   |
| Pj8               | -1.6±0.5 | -3.2±0.3 | 1.1e-03                                   |
| Pj9               | -1.0±0.3 | -3.2±0.5 | 2.6e-03                                   |
| Pj11              | -0.9±0.3 | -3.6±0.5 | 2.5e-03                                   |
| Pj13              | -0.3±0.7 | -2.5±0.7 | 7.4e-04                                   |
| median            | -0.9±0.2 | -3.2±0.3 | 2.0e-03±9.3e-04                           |

## Equatorward

| Perijove's passes | Slope 1  | Slope 2  | Transition wavenumber (km <sup>-1</sup> ) |
|-------------------|----------|----------|---|
| Pj4               | -1.3±0.3 | -3.6±0.4 | 2.1e-03                                   |
| Pj6               | -1.3±0.4 | -3.1±0.3 | 1.8e-03                                   |
| Pj8               | -1.2±0.3 | -3.5±0.4 | 2.0e-03                                   |
| Pj9               | -1.0±0.3 | -3.4±0.3 | 1.9e-03                                   |
| Pj11              | -1.1±0.3 | -3.6±0.4 | 2.1e-03                                   |
| Pj13              | -1.9±0.3 | -3.0±0.3 | 1.7e-04                                   |
| median            | -1.2±0.2 | -3.4±0.2 | 2.0e-03±1.3e-04                           |

Figure 1.

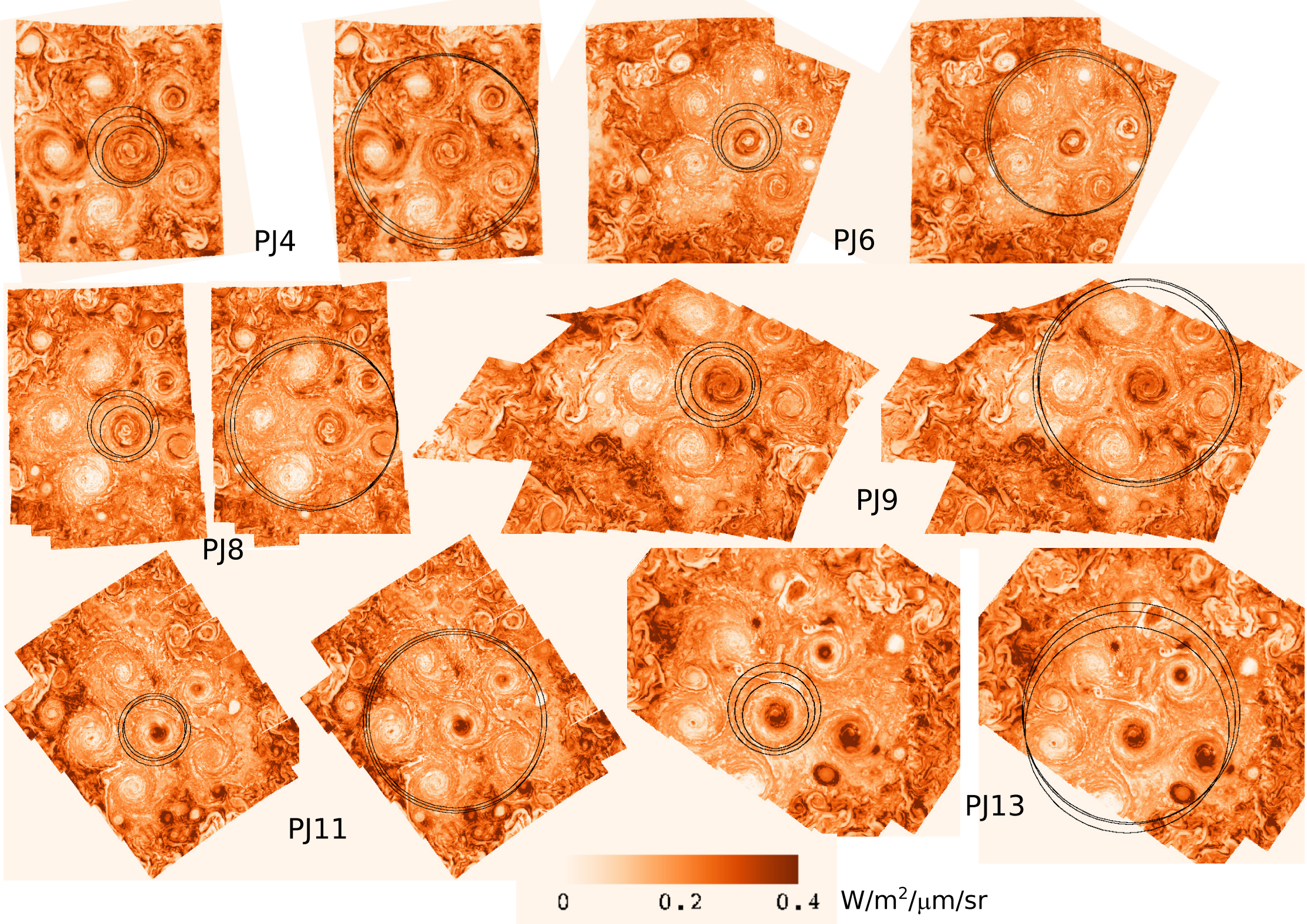


Figure 2.

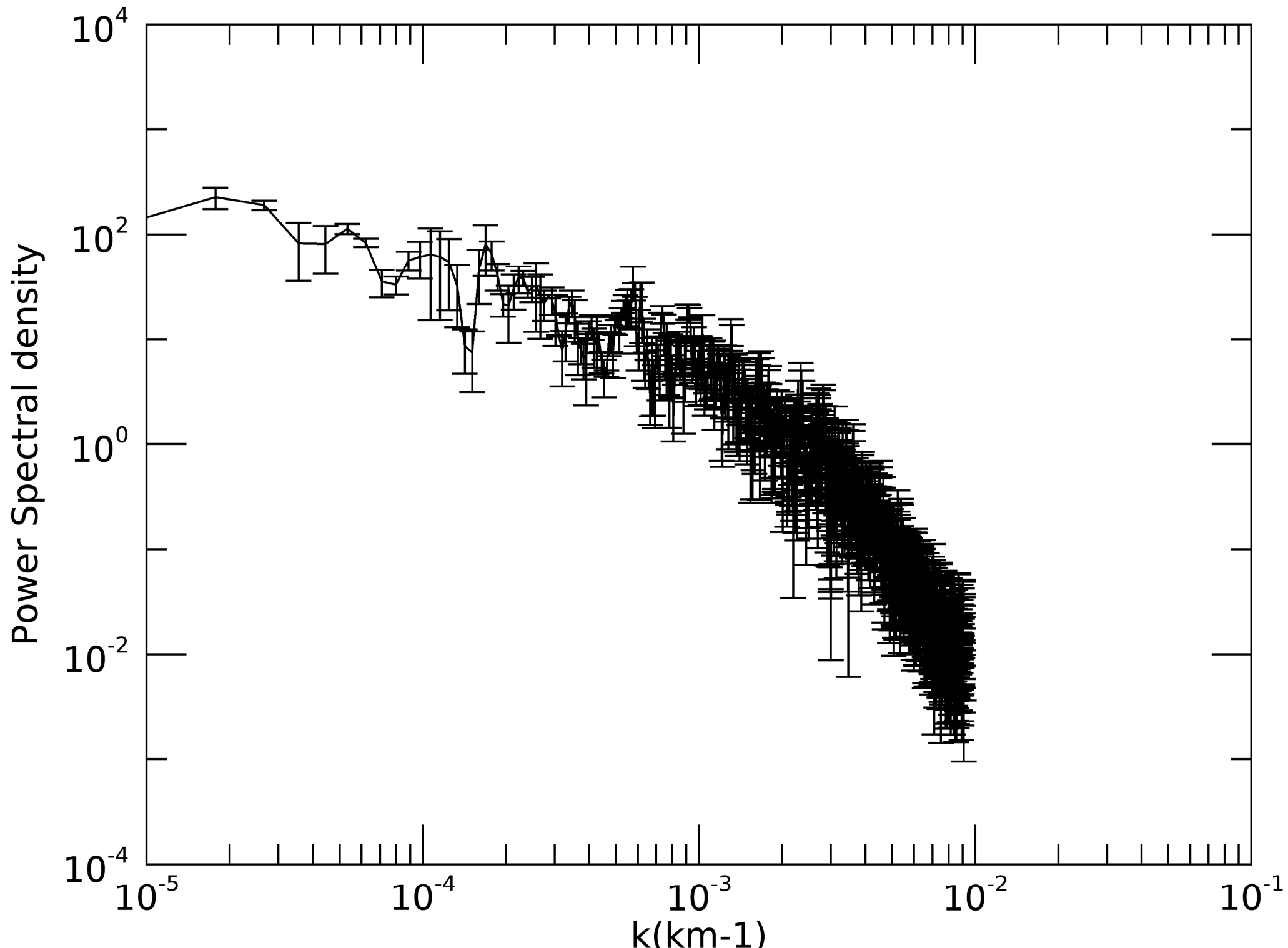
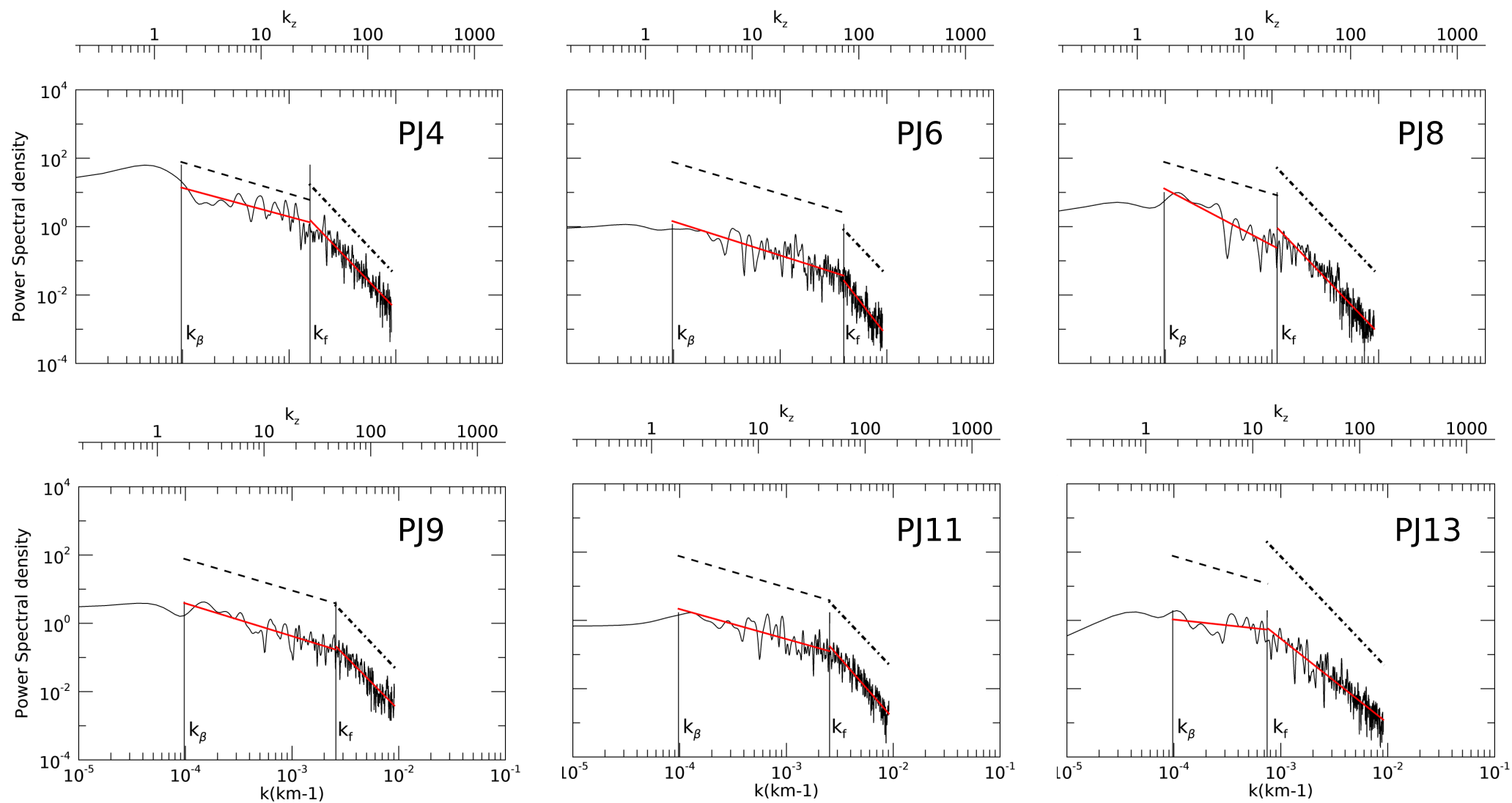
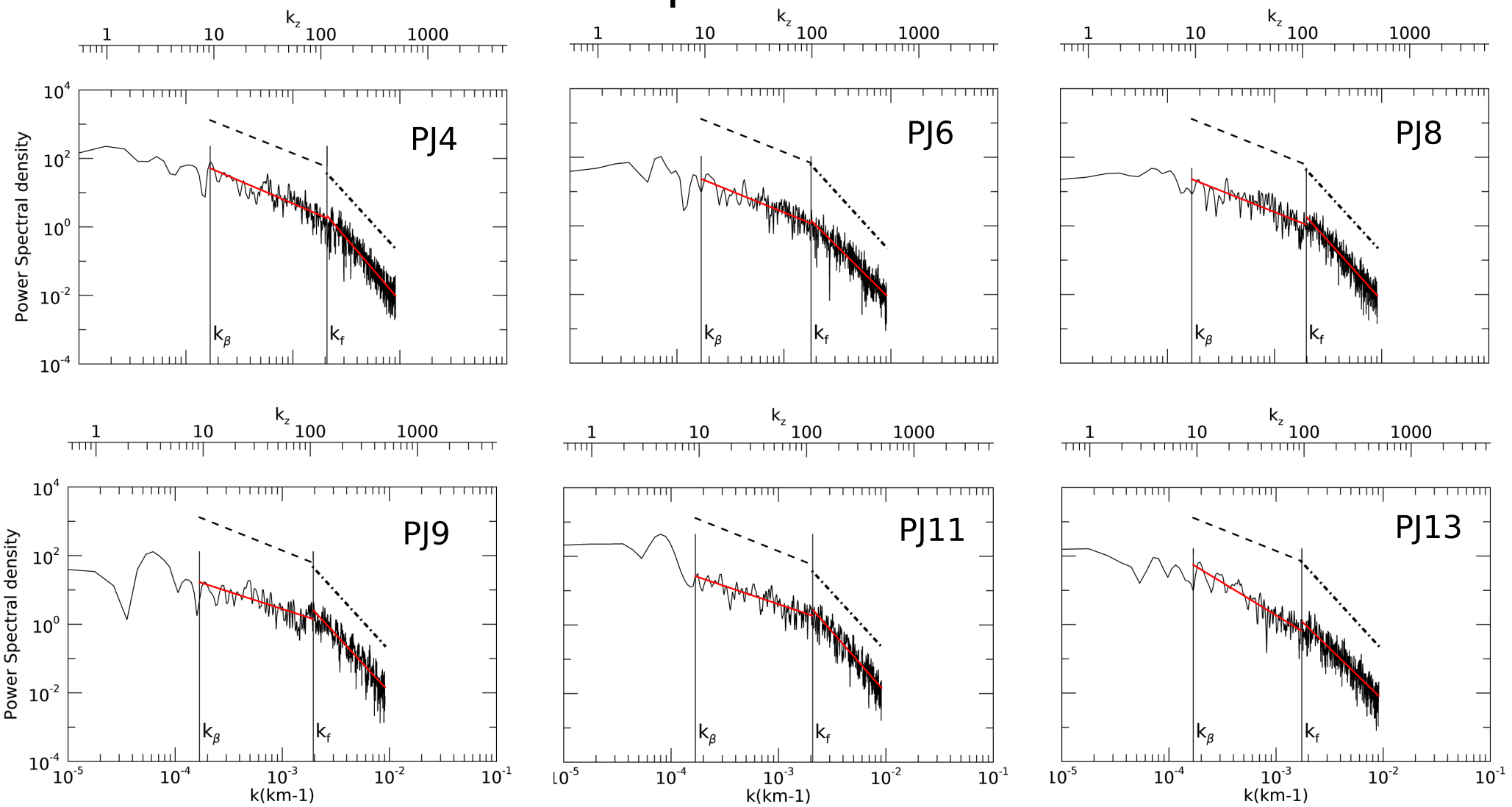


Figure 3.

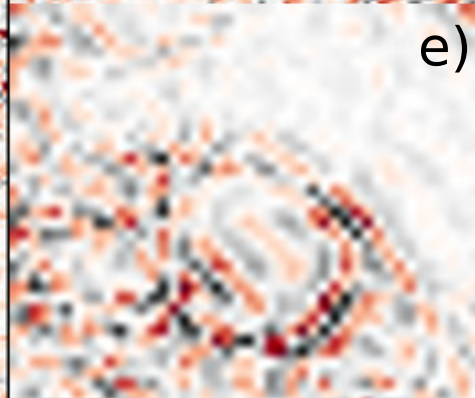
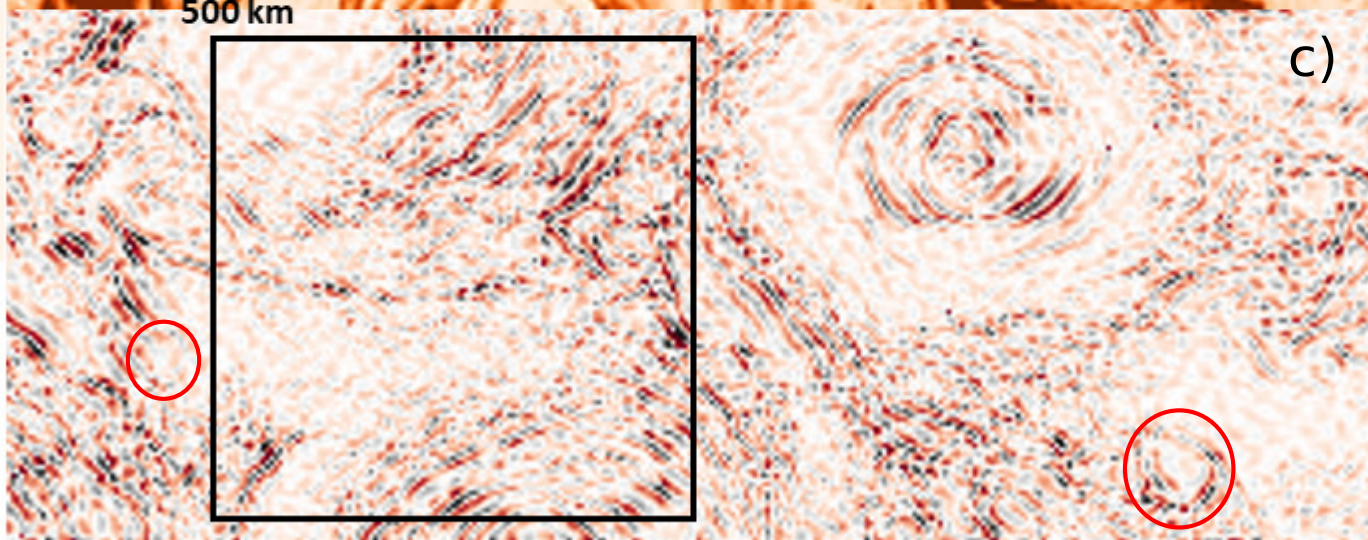
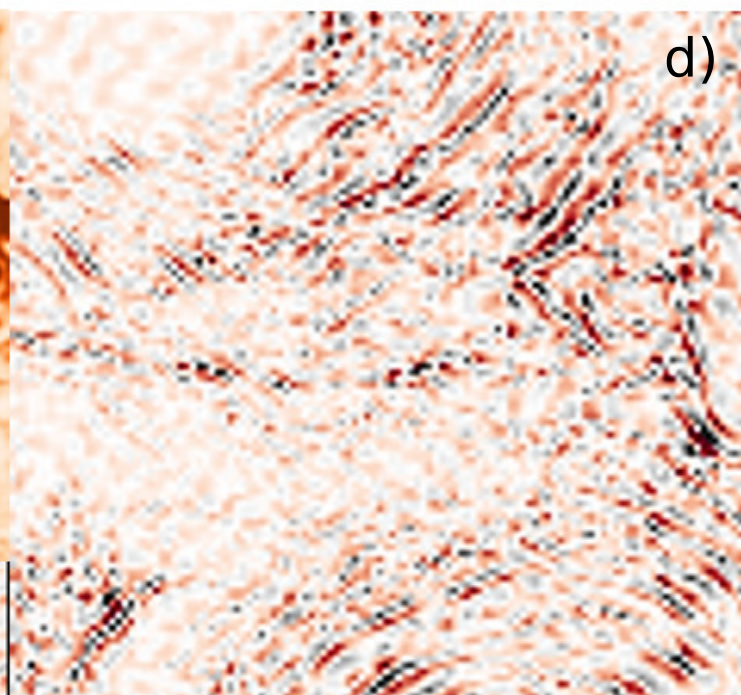
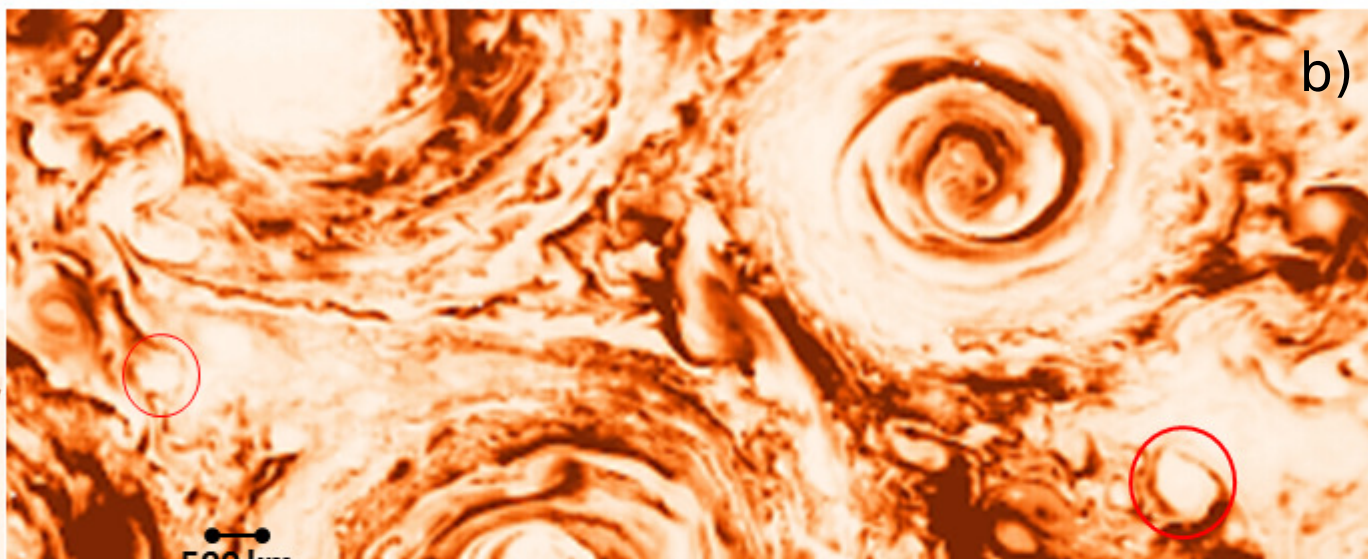
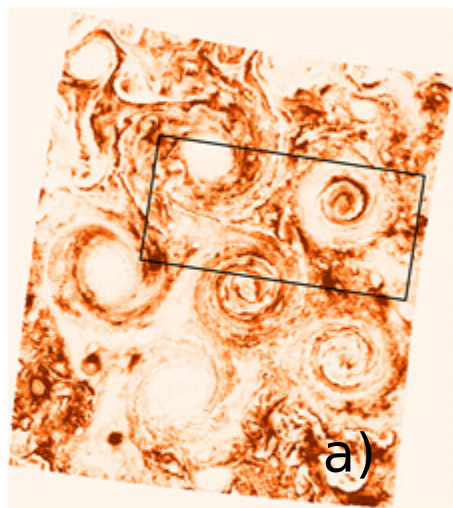
# Poleward



# Equatorward



**Figure 4.**



$W/m^2/\mu m/sr$